MEASURING THE OBLATENESS AND ROTATION OF TRANSITING EXTRASOLAR GIANT PLANETS

JASON W. BARNES AND JONATHAN J. FORTNEY
Department of Planetary Sciences, University of Arizona, Tucson, AZ 85721; jbarnes@c3po.lpl.arizona.edu, jfortney@lpl.arizona.edu

ABSTRACT

We investigate the prospects for characterizing extrasolar giant planets by measuring planetary oblateness from transit photometry and inferring planetary rotational periods. The rotation rates of planets in the solar system vary widely, reflecting the planets' diverse formational and evolutionary histories. A measured oblateness, assumed composition, and equation of state yields a rotation rate from the Darwin-Radau relation. The light curve of a transiting oblate planet should differ significantly from that of a spherical one with the same cross-sectional area under identical stellar and orbital conditions. However, if the stellar and orbital parameters are not known a priori, fitting for them allows changes in the stellar radius, planetary radius, impact parameter, and stellar limb-darkening parameters to mimic the transit signature of an oblate planet, diminishing the oblateness signature. Thus, even if HD 209458b had an oblateness of 0.1 instead of our predicted 0.003, it would introduce a detectable departure from a model spherical light curve at the level of only one part in 10^5. Planets with nonzero obliquity break this degeneracy because their ingress light curve is asymmetric relative to that from egress and their best-case detectability is of order 10^{-4}. However, the measured rotation rate for these objects is nonunique due to degeneracy between obliquity and oblateness and the unknown component of obliquity along the line of sight. Detectability of oblateness is maximized for planets transiting near an impact parameter of 0.7, regardless of obliquity. Future measurements of oblateness will be challenging because the signal is near the photometric limits of current hardware and inherent stellar noise levels.

Subject headings: occultations — planetary systems — planets and satellites: general —
planets and satellites: individual (HD 209458b)

1. INTRODUCTION

Discovery of the transiting extrasolar planet HD 209458b (Charbonneau et al. 2000; Henry et al. 2000) has provided one mechanism for researchers to move beyond the discovery and into the characterization of extrasolar planets. Precise *Hubble Space Telescope* (*HST*) measurements of HD 209458b's transit light curve revealed the radius $(1.347 \pm 0.060) R_{\rm Jup}$ and orbital inclination $(86°.68 \pm 0°.14)$ from impact parameter 0.508 of the planet, which, along with radial velocity measurements, unambiguously determine the planet's mass $(0.69 \pm 0.05\ M_{\rm Jup})$ and density $(0.35\ {\rm g\ cm^{-3}};$ Brown et al. 2001). Of the over 100 extrasolar planets discovered so far, this large radius makes HD 209458b the only one empirically determined to be a gas giant.

Knowledge of a planet's cross-sectional area provides a zeroth order determination of its geometry, and the *HST* photometry is precise enough to constrain the shape of HD 209458b to be rounded to first order. While a planet transits the limb of its star, the rate of decrease in apparent stellar brightness is related to the rate of increase in stellar surface area covered by the planet in the same time interval. We investigate whether it is possible to use this information to determine the shape of the planet to second order.

Rotation causes a planet's shape to be flattened or oblate by reducing the effective gravitational acceleration at the equator (as a result of centrifugal acceleration) and by redistributing mass within the planet (which changes the gravity field). Oblateness, f, is defined as a function of the equatorial radius ($R_{\rm eq}$) and the polar radius (R_p),

$$f \equiv \frac{R_{\rm eq} - R_p}{R_{\rm eq}} \ . \qquad (1)$$

For Jupiter and Saturn, high rotation rates and low densities result in highly oblate planets: $f_{\rm Jup} = 0.06487$ and $f_{\rm Sat} = 0.09796$, compared to $f_{\oplus} = 0.00335$.

An earlier investigation of the detectability of oblateness in transiting extrasolar planets was published by Seager & Hui (2002). Our work represents an improvement over Seager & Hui (2002) in the use of model fits to compare oblate and spherical planet transits, the use of the Darwin-Radau relation to associate oblateness and rotation, and a thorough investigation of the degeneracies involved in fitting a transit light curve.

In this paper, we investigate the reasons for measuring planetary rotation rates, the relationship between rotation rate and oblateness for extrasolar giant planets, the effect of oblateness on transit light curves, and the prospects for determining the oblateness of a planet from transit photometry.

2. EXOPLANETS AND ROTATION

While knowledge of a planet's mass and radius provides information regarding composition and thermal evolution, measurements of rotation and obliquity promise to constrain the planet's formation, tidal evolution, and tidal dissipation. What these data might reveal about a planet depends on whether the planet is unaffected by stellar tides, slightly affected by tides, or heavily influenced by tides.

2.1. *Tidally Unaffected*

The present-day rotation rate of a planet is the product of both the planet's formation and its subsequent evolution. Planets at sufficiently large distances from their parent stars

are not significantly affected by stellar tides; thus, these objects rotate with their primordial rates altered by planetary contraction and gravitational interactions between the planet, its satellites, and other planets. To the degree that a planet's rotational angular momentum is primordial, it may be diagnostic of the planet's formation. Planets formed in circular orbits from a protoplanetary disk inherit net prograde angular momentum from the accreting gas, resulting in rapid prograde rotation (Lissauer 1995). Planets that form in eccentric orbits receive less prograde specific angular momentum than planets in circular orbits, and as a result, they rotate at rates varying from slow retrograde up to prograde rotations similar to those of circularly accreted planets (Lissauer et al. 1997). Thus, comparing the current-day rotation rates for planets in circular and eccentric orbits may reveal whether extrasolar planets formed in eccentric orbits or acquired their eccentricity later from dynamical interactions with other planets or a disk.

The orientation of a planet's rotational axis relative to the vector perpendicular to the orbital plane, the planet's obliquity or axial tilt (t), can also provide insight into the planet's formation mechanism. Jupiter's low obliquity ($3°.12$) has been suggested as evidence that its formation was dominated by orderly gas flow rather than the stochastic impacts of accreting planetesimals (Lissauer 1993). Tidally unevolved extrasolar planets determined to have high obliquities could be inferred either to have formed differently than Jupiter or to have undergone large obliquity changes, as has been suggested for Saturn ($t = 26°.73$; Ward & Hamilton 2002).

2.2. Tidally Influenced

Tidal interaction between planets and their parent stars slows the rotation of those planets with close-in orbits (Guillot et al. 1996). This tidal braking continues until the net tidal torque on the planet becomes zero. Whether a planet reaches this end state depends on its age, radius, semimajor axis, and the planet-to-star mass ratio.

The rate of tidal braking also depends on the parameter Q, which represents the internal tidal dissipation within the planet. The value of Q is poorly constrained even for the planets in our own solar system (Goldreich & Soter 1966). Nevertheless, measurements of extrasolar planet rotation rates could constrain Q for these planets based on the degree of tidal evolution that has taken place (Seager & Hui 2002).

Tidal braking for objects with nonzero obliquity can, somewhat counterintuitively, act to increase an object's obliquity. Tidal torques reduce the component of a planet's angular momentum perpendicular to the orbital plane faster than they reduce the component of the planet's angular momentum in the orbital plane (Peale 1999). This occurs because at solstice the planet's induced tidal bulge is not carried away from the planet's orbital plane by planetary rotation. Therefore, for large fractions of the year, stellar tidal torques do not act to right the planet's spin axis, while torques that reduce the angular momentum perpendicular to the orbital plane act year-round. As a result, planets that have undergone partial tidal evolution can exhibit temporarily increased obliquity as the planet's rotation rate decreases. Eventually, such a planet reaches maximum obliquity and thereafter approaches synchronous rotation and zero obliquity simultaneously. Planets undergoing tidal evo-

lution may be expected to have higher obliquities on average than planets retaining their primordial obliquity.

2.3. Tidally Dominated

The end state of tidal evolution for planets in circular orbits is a 1:1 spin-orbit synchronization between the planet's rotation and its orbital period along with zero obliquity. However, most of the extrasolar planets discovered thus far are on eccentric orbits (Marcy, Cochran, & Mayor 2000). (We sometimes shorten "planets on eccentric orbits" to "eccentric planets," even though the eccentricity is not inherent to the planet.) Thus, these eccentric planets will never reach 1:1 spin-orbit coupling as a result of tidal evolution because the tidal torque (eq. [2]) on the planet from its star is much stronger (due to the r^{-6} dependence) near periapsis.

The tidal torque between a planet and star is given by (Murray & Dermott 2000)

$$\tau_{p-*} = -\frac{3}{2} \frac{k_2 \, G \, M_*^2 \, R^5}{Q \, r^6} \, \mathrm{sgn} \, (\Omega - \dot{\phi}) \, , \qquad (2)$$

where k_2 is the planet's Love number, R its radius, Ω its rotation rate (in radians per second), $\dot{\phi}$ the instantaneous orbital angular velocity (also in radians per second), and r the instantaneous distance between the planet and star. The function $\mathrm{sgn} \, (x)$ is equal to 1 if x is positive and -1 if x is negative. The magnitude of the stellar perturbation is proportional to GM_*^2, the product of the stellar mass (M_*) squared and the gravitational constant (G). The planet is spun down by tidal torques if its rotation is faster than its orbital motion ($\Omega > \dot{\phi}$), and it is spun up if its rotation is slower than the orbital motion ($\Omega < \dot{\phi}$).

If an eccentric planet were in a 1:1 spin-orbit state, it would be spun up by the star when its orbital angular velocity is greater than average near periapsis, and it would be spun down when the orbital angular velocity is low near apoapsis. The total positive tidal torque induced while the planet is in close will exceed the negative torque while it is far away, despite the shorter time spent near periapsis. Thus, to be in rotational equilibrium with respect to stellar tides, an eccentric, fluid planet must rotate faster than its mean motion.

The Earth's moon avoids this fate because it has a nonzero component of its quadrupole moment in its orbital plane. The torque that the Earth exerts on this permanent bulge exceeds the net tidal torque imparted on the moon due to its eccentric orbit, keeping the moon in synchronous rotation (Murray & Dermott 2000). Fluid planets, however, have no permanent quadrupole moment and thus have no restoring torque competing with the stellar tidal torques (Greenberg & Weidenschilling 1984). Tidal evolution ceases for these bodies when the net torque per orbit is zero, which can be achieved only by supersynchronous rotation.

The precise rotation rate necessary to balance the tidal torques over the eccentric orbit depends on how Q varies with the tidal forcing frequency (the difference between the rotation rate and instantaneous orbital angular velocity, $\Omega_p - \dot{\phi}_p$). Conventionally, Q has been assumed to be either independent of the forcing frequency or inversely proportional to it (Goldreich & Peale 1968). The resulting equilibrium spin-orbit ratios as a function of eccentricity for each of these cases are plotted in Figure 1.
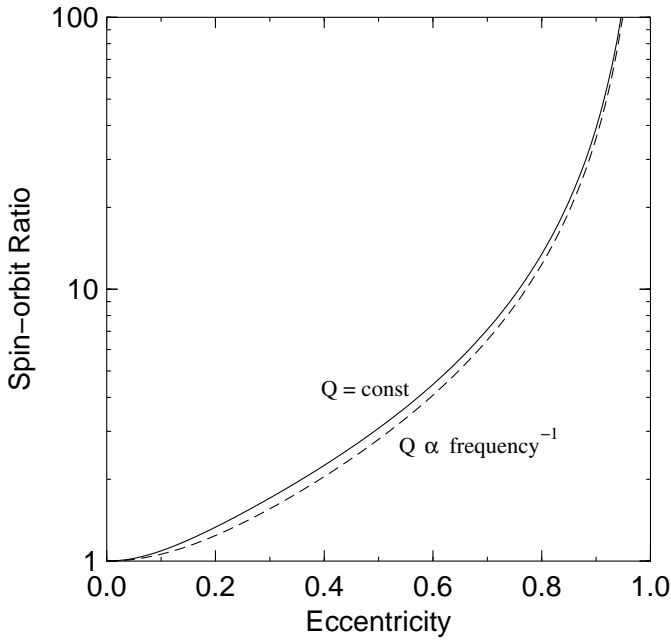
FIG. 1.—Spin to orbital mean motion ratios for tidally evolved fluid planets in equilibrium. *Solid line*: Ratio as calculated under the assumption of a frequency-independent tidal dissipation factor Q. *Dashed line*: Calculated assuming $Q \propto$ frequency^{-1}. Under these assumptions, extremely eccentric planet HD 80606b ($e = 0.93$) would, if allowed to come to tidal equilibrium, rotate over 90 times faster than its mean orbital motion!

Probably both of these assumptions for the behavior of Q are too simple. In particular, if the behavior of Q changes under a varying tidal forcing frequency ($\Omega_p - \dot{\phi}_p$ is a function of time), then the tidal equilibrium rotation rate would differ significantly from that plotted in Figure 1. Measurement of rotational rates of eccentric extrasolar planets in tidal equilibrium could, in principle, either differentiate between these two models or suggest other frequency dependences, shedding light on the yet unknown mechanism for tidal dissipation within giant planets.

3. ROTATION AND OBLATENESS

Rotation affects the shape of a planet via two mechanisms. Gravity must provide centripetal acceleration—thus the higher velocity at the equator causes the planet to bulge by transfer of mass from polar regions—and, secondarily,

the redistributed mass alters the planet's gravitational field and attracts even more mass toward the equatorial plane. The ratio of the required centripetal acceleration at the equator to the gravitational acceleration, q, represents the relative importance of the centripetal acceleration term as

$$q = \frac{\Omega^2 R_{\mathrm{eq}}^3}{GM_p} , \qquad (3)$$

where Ω is the rotation rate in radians per second, M_p is the mass of the planet, and R_{eq} is the planet's equatorial radius (Murray & Dermott 2000).

We use the Darwin-Radau relation to relate rotation and oblateness accounting for the gravitational pull of the shifted mass (Murray & Dermott 2000),

$$\mathbb{C} \equiv \frac{C}{M_p R_{\mathrm{eq}}^2} = \frac{2}{3}\left[1 - \frac{2}{5}\left(\frac{5}{2}\frac{q}{f} - 1\right)^{1/2}\right] , \qquad (4)$$

where C is the planet's moment of inertia around the rotational axis and $\mathbb{C}$ is shorthand for $CM_p^{-1}R_{\mathrm{eq}}^{-2}$. The Darwin-Radau relation is exact for uniform density bodies ($\mathbb{C} = 0.4$) but is only an approximation for gas giant planets ($\mathbb{C} \sim 0.25$; Hubbard 1984).

By combining equations (3) and (4), we arrive at a relation for rotation rate, Ω, as a function of oblateness, f,

$$\Omega = \sqrt{\frac{fGM_p}{R_{\mathrm{eq}}^3}\left[\frac{5}{2}\left(1 - \frac{3}{2}\mathbb{C}\right)^2 + \frac{2}{5}\right]} . \qquad (5)$$

For our solar system, the Darwin-Radau relation yields rotation periods accurate to within a few percent (Table 1) using model-derived moments of inertia from Hubbard & Marley (1989).

Extending the Darwin-Radau relation to extrasolar planets requires estimation of the appropriate moment of inertia coefficients, $\mathbb{C}$, for those planets. For transiting planets whose masses and radii are known, we use a self-consistent hydrodynamic model of the planet and assumptions about its composition to estimate $\mathbb{C}$ following Fortney & Hubbard (2003). To first order, $\mathbb{C}$ is independent of oblateness due to similar symmetry around the rotational axis so our hydrodynamic model does not need to explicitly incorporate oblateness. The Darwin-Radau relation and spherically symmetric hydrodynamic models provide sufficient precision for the current work; however, to estimate the oblateness as a function of rotation more robustly, a two-

TABLE 1
DARWIN-RADAU IN THE SOLAR SYSTEM

Planet	f	$\mathbb{C}$	Calculated Period (hr)	Actual Period (hr)	Error (%)
Jupiter........	0.06487	0.26401[a]	10.1609	9.92425	2.38
Saturn........	0.09796	0.22037[a]	10.8817	10.6562	2.12
Uranus.......	0.02293	0.2268 [a]	16.6459	17.24	3.45
Neptune.....	0.01708	0.23 [b]	16.8656	16.11	4.69
Earth	0.00335	0.3308	23.8808	23.9342	0.223

NOTE.—Comparison of calculated rotation rates from the Darwin-Radau approximation (eq. [4]) to actual rotation rates for selected planets in our solar system.
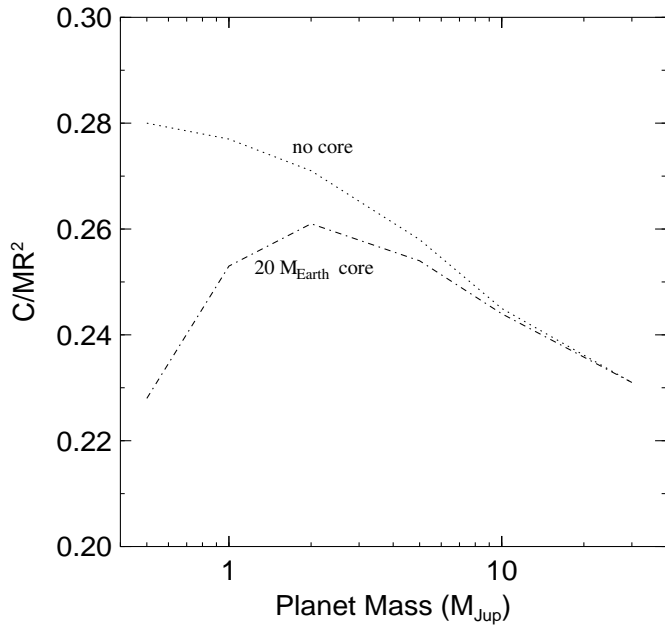[a] Hubbard & Marley 1989.
[b] Assumed.

FIG. 2.—Moment of inertia coefficient, $\mathbb{C}$, as a function of planet mass for hypothetical generic $1.0 R_{\mathrm{Jup}}$ extrasolar giant planets. Extrasolar giant planets may or may not possess rocky cores depending on their formation mechanism, so we plot $\mathbb{C}$ for both no core (*upper curve*) and an assumed 20 $M_\oplus$ core (*lower curve*).

dimensional interior model involving both rotational and gravitational forces should be used (e.g., Hubbard & Marley 1989).

Under the spherically symmetric assumption, we calculate the $\mathbb{C}$ of Jupiter to be 0.277 with no core and 0.253 with a 20 $M_\oplus$ core, and we calculate the $\mathbb{C}$ of Saturn to be 0.225 with a core. (We are unable to calculate the interior structure of Saturn without a core due to deficiencies in our knowledge of the equation of state.) Using these moments of inertia instead of the measured ones listed in Table 1 yields similar rotation errors of a few percent. We apply our model to generic 1.0 R_{Jup} extrasolar giant planets of varying masses and architectures in Figure 2.

For HD 209458b, our models calculate $\mathbb{C}$ to be 0.218 with no core and 0.185 with a 20 $M_\oplus$ core. To estimate the oblateness of HD 209458b assuming synchronous rotation, we rearrange equation (5) to solve for f,

$$f = \frac{\Omega^2\, R^3}{G\, M_p}\left[\frac{5}{2}\left(1 - \frac{3}{2}\mathbb{C}\right)^2 + \frac{2}{5}\right]^{-1}, \qquad (6)$$

and then use the synchronous rotation rate $\Omega = 2.066 \times 10^{-5}$ radians s^{-1} to obtain $f = 0.00285$ with no core and $f = 0.00256$ with a 20 $M_\oplus$ core. These results imply an equator-to-pole radius difference of $\sim$200 km, which, although small, is still comparable to the atmospheric scale height at 1 bar, $\sim$700 km.

Showman & Guillot (2002) suggest that zonal winds on HD 209458b may operate at speeds up to $\sim$2 km s^{-1} in the prograde direction, and Showman & Guillot (2002) go on to show that these winds might then spin up the planet's interior, possibly to commensurate speeds of several hundred m s^{-1} up to a few km s^{-1} (though the model of Showman & Guillot 2002 does not treat the outer layers and interior self-

consistently). This speed is a nonnegligible fraction of the orbital velocity around the planet at the surface, 30 km s^{-1}, and is also comparable to the planet's rotational velocity at the equator, 2.0 km s^{-1}. As such, if radiatively driven winds prove to be important on HD 209458b, they would affect the planet's oblateness. We use the rotation rate implied by the Showman & Guillot (2002) calculations to provide an upper limit for the expected oblateness of HD 209458b. If the entire planet was spinning at its synchronous rate plus 2 km s^{-1} at the cloud tops, the rotational period would be halved to 1.8 days, with a corresponding oblateness of 0.0109 and 0.0098 for the no-core and core models, respectively.

During revision of this paper, Konacki et al. (2003) announced the discovery of a second transiting planet. This new planet, OGLE-TR-56b, has a radius of $1.3 R_{\mathrm{Jup}}$, a mass of $0.9 R_{\mathrm{Jup}}$, and an extremely short orbital period of 1.2 days. Although these parameters are less constrained than those for HD 209458b, we proceed to calculate that the oblateness of this new object should be 0.017 with no core and 0.016 with a 20 $M_\oplus$ core, for $\mathbb{C}$ of 0.228 and 0.204, respectively.

Current ground-based transit searches detect low-luminosity objects such as brown dwarfs and low-mass stars in addition to planets. However, the high surface gravity for brown dwarfs and lower main-sequence stars leads to low values of q and very small oblatenesses for those objects. For a $13 M_{\mathrm{Jup}}$ brown dwarf with $1.0 R_{\mathrm{Jup}}$ in an HD 209458b–like 3.52 day orbit, the expected oblateness is only 0.00007. Measuring oblateness will therefore be practical only for transiting planets and not for other transiting low-luminosity bodies.

We also note that the measurement of oblateness along with an independent measurement of a planet's rotation rate Ω would determine the planet's moment of inertia. This would provide a direct constraint on the planet's internal structure, possibly allowing inferences regarding the planet's bulk helium fraction and/or the presence of a rocky core.

4. OBLATENESS AND TRANSIT LIGHT CURVES

4.1. *Transit Anatomy*

Brown et al. (2001, hereafter BCGNB) investigated the detailed structure of a transit light curve while studying the *HST* light curve of the HD 209458b transit. Figure 3 relates transit events to corresponding features in the light curve, modeled after BCGNB's Figure 4. The flux from the star begins to drop at the onset of transit, known as the first contact. As the planet's disk moves onto the star, the flux drops further until at second contact, the entire planet disk blocks starlight. Third contact is the equivalent of second contact during egress, and fourth contact marks the end of the transit. Due to stellar limb darkening, the planet blocks a greater fraction of the star's light at mid-transit than at the second and third contacts, leading to curvature at the bottom of the transit light curve.

For a given stellar mass (M_*), the total transit duration, l, is a function of the transit chord length and the orbital velocity. We assume a circular orbit that fixes the planet's orbital velocity. The chord length depends on the stellar radius, R_*, and the impact parameter, b. The impact parameter relates to i, the inclination of the orbital plane relative
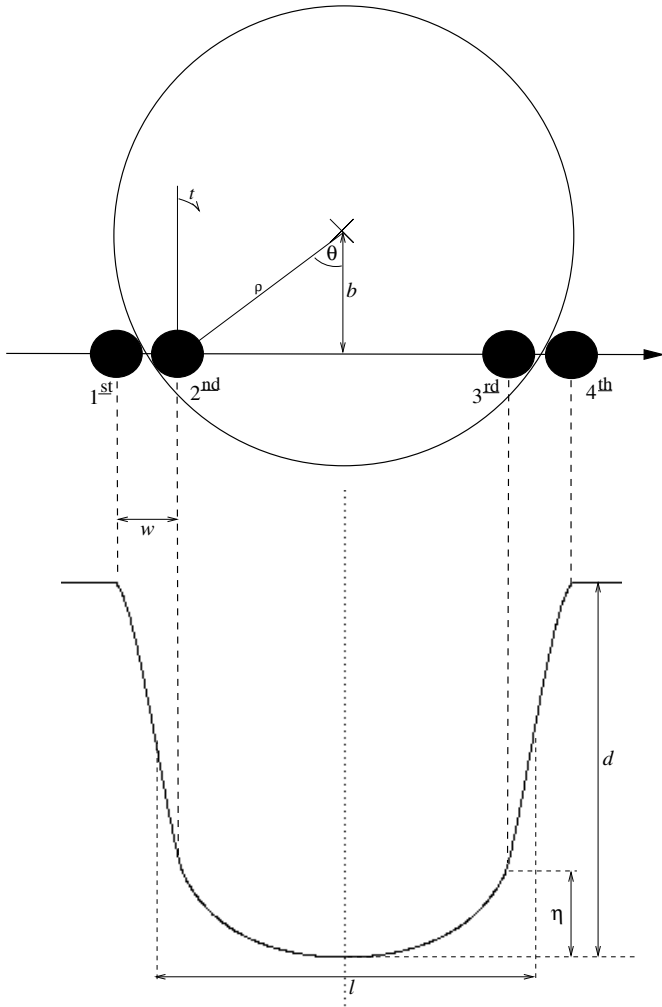
Fig. 3.—Anatomy of a transit after BCGNB

to the plane of the sky, as

$$b = \frac{|a \cos(i)|}{R_*} , \qquad (7)$$

where a is the semimajor axis of the planet's orbit.

The duration of ingress and egress, w, is the time between first and second contact and is a function of R_p, R_*, and b (or i). Transits with $b \sim 0$ have smaller w than transits with higher b. For transits with $b \sim 1$, called grazing transits, w is undefined because there is no second or third contact.

The total transit depth, d, fixes the ratio R_p/R_*, where R_p is the radius of the planet (except in the case of grazing transits).

The magnitude of the curvature at the bottom of the transit light curve, η, determines the stellar limb darkening. We use limb-darkening parameters u_1 and u_2, or c_1 and c_2, which we define mathematically in § 4.2.

4.2. Methods

We calculate theoretical transit light curves by comparing the amount of stellar flux blocked by the planet to the total stellar flux. The relative emission intensity across the disk of the star is greatest in the center and lowest along the edges as a result of limb darkening. Many parameterizations of limb darkening exist (see Claret 2000); however, we use the

one proposed by BCGNB because it is the most appropriate for planetary transits.

The emission intensity at a given point on the stellar disk, I, is parameterized as a function of $\mu = \cos[\sin^{-1}(\rho/R_*)]$, where ρ is the projected (apparent) distance between the center of the star and the point in question. BCGNB defined a set of two limb-darkening coefficients, which we call c_1 and c_2, that are equivalent to

$$\frac{I(\mu)}{I(1)} = 1 - c_1 \frac{(1-\mu)(2-\mu)}{2} + c_2 \frac{(1-\mu)\mu}{2} . \qquad (8)$$

The advantage of this limb-darkening function is that c_1 describes the magnitude of the darkening, while c_2 is a correction for curvature. This makes the BCGNB coefficients particularly useful for fitting transit observations because a good fit to data can be achieved by fitting only for the c_1 coefficient.

Our algorithm for calculating the light curve takes advantage of the symmetry inherent in the problem: that $I(\mu)$ depends only on ρ and not on the angle around the star's center, θ. We evaluate the apparent stellar flux at time τ, $F(\tau)$, relative to the out-of-transit flux F_0, by subtracting the amount of stellar flux blocked by the planet from F_0,

$$F_0 = \int_0^{R_*} 2\pi I(\rho) \, d\rho , \qquad (9)$$

$$F_{\text{blocked}} = \int_0^{R_*} 2\pi I(\rho) \, x(\rho, \tau) \, d\rho , \qquad (10)$$

and

$$F(\tau) = \frac{F_0 - F_{\text{blocked}}}{F_0} , \qquad (11)$$

where $x(\rho, \tau)$ is the fraction of a ring of radius ρ and width $d\rho$ covered by the planet at time τ. In effect, we split the star up into infinitesimally small rings and add up the fluxes in equation (9), then we determine how much of each of these rings is covered by the planet in equation (10). We calculate the integrals numerically using Romberg's method (Press et al. 1992): $x(r, t)$ is evaluated numerically as well. There is no closed-form general analytical solution to the intersection of an ellipse and a circle.

This algorithm is more efficient than the raster method used by Hubbard et al. (2001) for planets treated as opaque disks because the use of symmetry and Romberg integration minimize the number of computations of the stellar intensity, $I(\mu)$.

4.3. Results

To illustrate the effect oblateness has on a transit light curve, we calculate the difference between the light curve of an oblate, zero-obliquity planet and that of a spherical planet with the same cross-sectional area. For familiarity, we adopt the transit parameter values measured by BCGNB for the HD 209458b transit: $R_p = 1.347 R_{\text{Jup}}$, $R_* = 1.146$ $R_\odot$, and $c_1 = 0.640$. Plots of the oblate-spherical differential as a function of impact parameter are shown in Figure 4.

For nearly central transits, an oblate planet encounters first contact before, and second contact after, the equivalent spherical planet. This situation causes the oblate planet's transit light curve initially to dip below that of the spherical planet. However, near the time when the planet center is
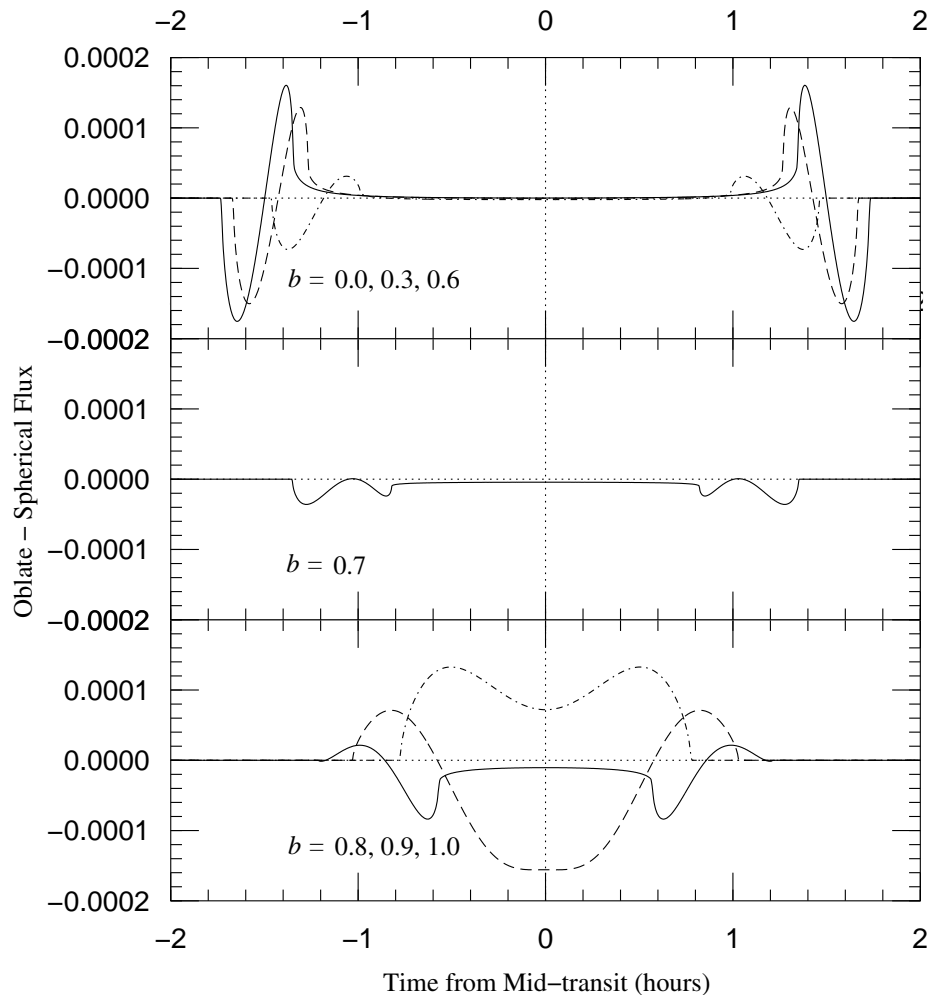
FIG. 4.—Oversimplified model of the effect of oblateness on a transit light curve. We plot the differences between the light curve of an oblate planet and the light curve of a spherical planet with the same cross-sectional area, $F_{f=0.1}(t) - F_{f=0.0}(t)$ while holding all other transit parameters, R_*, R_p, b, and c_1 the same and setting these values equal to those values measured by BCGNB for HD 209458b. *Top panel*: Light curve differential for impact parameters $b = 0.0$ (*solid line*), $b = 0.3$ (*dashed line*), and $b = 0.6$ (*dot-dashed line*). An oblate planet for $b < 0.7$ encounters first contact before and second contact after the equivalent spherical planet, resulting in the initial negative turn for $F_{f=0.1}(t) - F_{f=0.0}(t)$ and subsequent positive section of the curve for these impact parameters. *Bottom panel*: Differential light curve for $b = 0.8$ (*solid line*), $b = 0.9$ (*dashed line*), and $b = 1.0$ (*dot-dashed line*). For $b > 0.7$, under otherwise identical conditions, an oblate planet first encounters the limb of the star after the equivalent spherical planet and last touches the limb later on ingress. For $b = 0.9$, because $R_p > 0.1R_*$, there is no second contact; i.e., the transit is partial, so the flux differential does not return to near zero, even at mid-transit. *Middle panel*: Light curve differential at the changeover point between these two regimes, where $b = 0.7$.

covering the limb of the star, each planet blocks the same apparent stellar area and the stellar flux difference is zero. As the two hypothetical transits approach second contact, this trend reverses and the spherical planet starts blocking more light than the oblate one until the oblate planet nearly catches up at second contact. Between second and third contacts, the light curve differences are slightly nonzero because the two planets cover areas of the star with differing amounts of limb darkening. The light curves are symmetric such that these effects repeat themselves in reverse upon egress.

At high-impact parameters (nearly grazing planet transits), the opposite occurs. First contact for the oblate planet occurs after that for the spherical planet because the point of first contact on the planet is closer to the pole than to the equator. In this scenario, the oblate planet's transit flux starts higher than, becomes equivalent to, and then drops below that of the spherical planet before returning to near zero for the times between second and third contact. In the case of a grazing transit, this sequence is truncated because there is no second or third contact.

The boundary between these two regions occurs when the local oblate planet radius at the point of first contact is equal to R_{ea}, the radius of the equivalent spherical planet. For planets that are small compared with the sizes of their stars ($R_p \ll R_*$) and that have low oblateness ($f \lesssim 0.1$), this transition occurs when $\theta = \pi/4$ (from Fig. 3) and $b = 2^{-1/2} = 0.707$. The flux difference between transits of oblate planets and that for spherical planets, all else being equal, is at a minimum at this point and deviates from zero because the rate of change in stellar area covered is different for the two planets. First, second, third, and fourth contacts all occur at nearly the same time for each planet. However, if all else is not equal, as is usually the case since the stellar parameters are poorly constrained, then this result is misleading and does not represent the detectability of planetary oblateness.

5. TRANSIT LIGHT CURVES AND EXOPLANETS

To test whether these flux differences are detectable, we use a Levenberg-Marquardt curve-fitting algorithm adapted from Press et al. (1992) to fit model transits to both the *HST* HD 209458b light curve and hypothetical model-generated light curves by minimizing χ^2. As a test, we fit the *HST* HD 209458b transit light curve and obtain $R_* = 1.142\ R_\odot$, $R_p = 1.343 R_{\rm Jup}$, $i = 86°.72$ ($b = 0.504$), $c_1 = 0.647$, and $c_2 = -0.065$ with a reduced χ^2 of 1.05, consistent with the values obtained by BCGNB.

In order for planetary oblateness to have a noticeable effect on a transit light curve, it must be distinguishable from the light curve of a spherical planet. For a spherical planet transit model, the combination of transit parameters that correspond to the light curve that best simulates the data from an actual oblate planet transit become the measured values, and these measured quantities may not be similar to the actual values. Therefore, to consider the detectability of planetary oblateness, we compare oblate planet transit light curves to those of the best-fit spherical planet light curve

instead of to the light curve of a planet that differs from the actual values only in the oblateness parameter (as we did in § 4.3).

5.1. *Zero Obliquity*

We compare a model transit of an oblate planet ($f = 0.1$) with zero obliquity, as is the case for a tidally evolved planet, to the transit of the *best-fit* spherical planet in Figures 5 and 6. The oblate planet transit signature is muted in each when compared to Figure 4 due to a degeneracy between the fitted parameters R_*, R_p, b, and the oblateness f. This degeneracy is introduced by the unconstrained nature of the problem; in essence, we are trying to solve for five free parameters, R_*, R_p, b, c_1, and f, given just four constraints, d, w, l, and η, assuming (as BCGNB did) knowledge of the stellar mass M_*. Without assuming a value for M_*, absolute timescales for the problem vanish, yielding a similar conundrum of solving for R_p/R_*, b, c_1, and f given only d, η, and w/l. The previous two sentences are intended to be
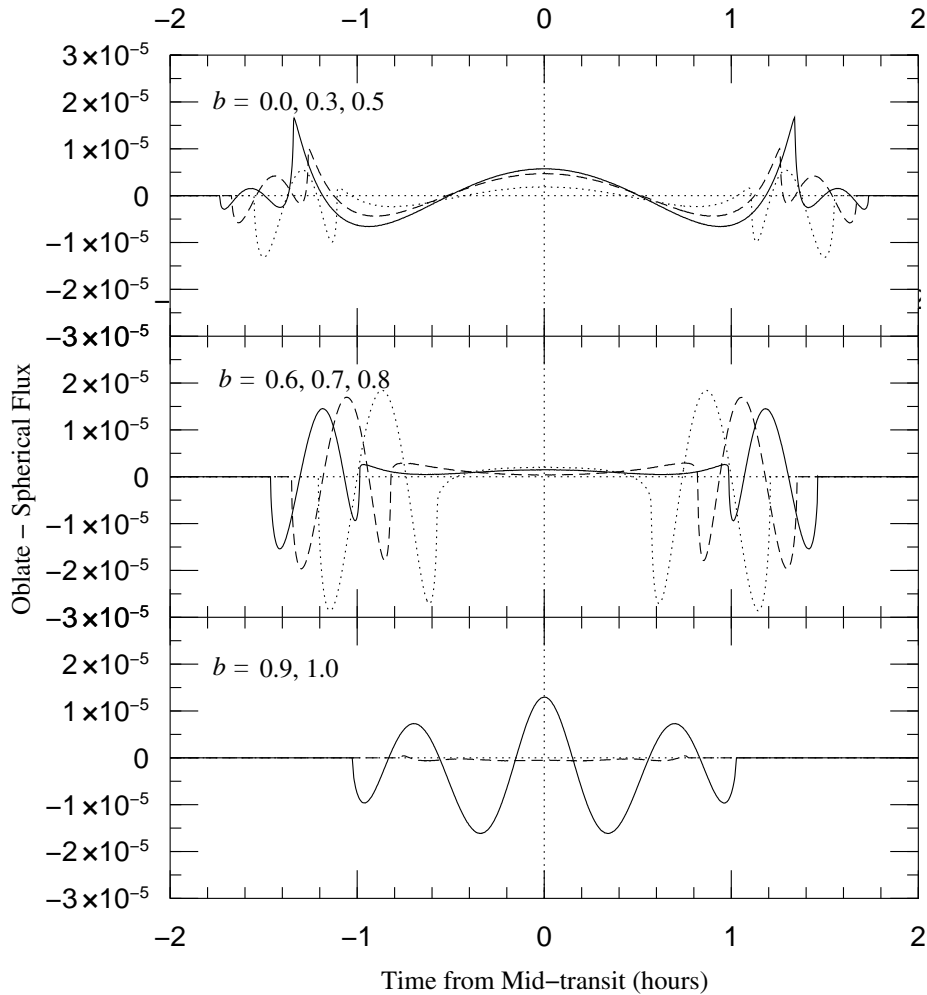

Fig. 5.—Detectable difference between the light curve of an oblate ($f = 0.1$) planet and the best-fit spherical model, fitting for R_*, R_p, b, and c_1. Higher b combined with larger values for R_* and R_p simulate the lengthened ingress and egress of an oblate planet, diminishing the difference between oblate and spherical planets from Fig. 4 for planets with $b < 0.7$ (*top panel*: *solid line*, $b = 0.0$; *dashed line*, $b = 0.3$; *dotted line*, $b = 0.5$). For planets near $b = 0.7$, the length of ingress and egress cannot be simulated by higher b, and as a result, the transit signal is highest for these planets (*middle panel*: *solid line*, $b = 0.6$; *dashed line*, $b = 0.7$; *dotted line*, $b = 0.8$). Above the critical value, $b > 0.7$, the oblate planet's signal can be simulated by lowering b for the spherical planet fit, reducing the detectability of oblateness (*bottom panel*: *solid line*, $b = 0.9$; *dashed line*, $b = 1.0$). It is very difficult to determine the oblateness for planets involved in grazing transits ($b \sim 1.0$). The magnitude of the detectability difference is proportional to f to first order; hence, to estimate the detectability of a planet with arbitrary oblateness, multiply the differences plotted here by $(f/0.1)(R_p^2/R_{\rm HD\ 209458b}^2)$.
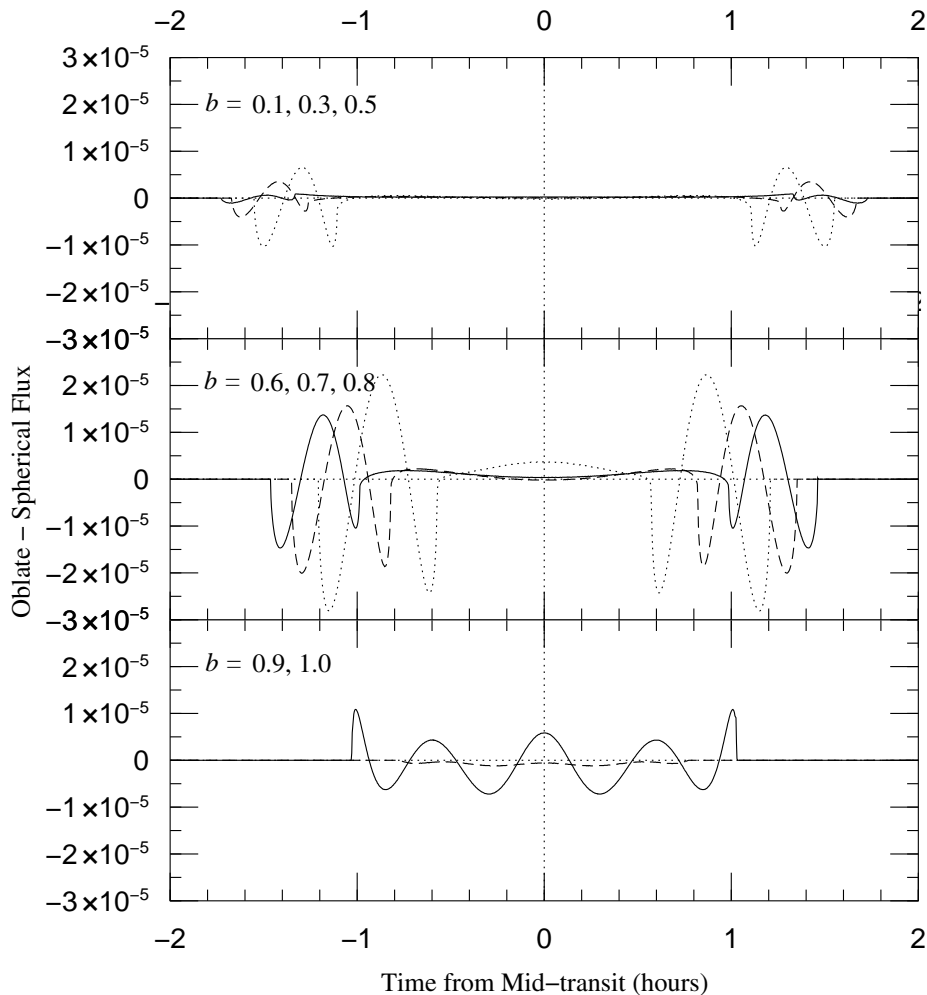
FIG. 6.—Detectable difference between the light curve of an oblate ($f = 0.1$) planet and its best-fit spherical model with five parameters: R_*, R_p, b, c_1, and c_2. As in Fig. 5, differing values for R_*, R_p, and b for a spherical planet transit can allow it to mimic the transit of an oblate planet. With the addition of c_2, the fit is much better for planets transiting at low impact parameter. (*Top panel*: solid line, $b = 0.0$; *dashed line*, $b = 0.3$; *dotted line*, $b = 0.5$. *Middle panel*: solid line, $b = 0.6$; *dashed line*, $b = 0.7$; *dotted line*, $b = 0.8$. *Bottom panel*: solid line, $b = 0.9$; *dashed line*, $b = 1.0$.) The differences for the five-parameter, like those for the four-parameter, model vary as $(f/0.1)(R_p^2/R_{\mathrm{HD\ 209458b}}^2)$.

simplifications, as at higher photometric precision, more information about the conditions of the transit is available. Hereafter, we assume knowledge of M_*, though this analysis also could have been done without this assumption or with an assumed relation between M_* and R_*, as proposed by Cody & Sasselov (2002). Changes in R_*, R_p, and b mimic the signal of an oblate planet by altering the ingress and egress times while maintaining the total transit duration by keeping the chord length constant.

For planets transiting at low-impact parameter ($b < 0.7$), an oblate planet's longer ingress and egress (higher w from Fig. 3) are fitted better using a spherical model with a higher impact parameter than actual, thus lengthening the time between first and second contact. Since for a given star, transits at higher impact parameter have shorter overall duration, the best-fit spherical model has a larger R_* than the model used to generate the data to maintain the chord length and, thus, a larger R_p to maintain the overall transit depth.

Similarly, for simulated light-curve data from a transiting oblate planet at high-impact parameter ($b > 0.7$), the best-fit spherical model has a lower impact parameter than the simulated planet to increase the duration of ingress and

egress. For these planets, the fitted spherical parameters have smaller R_* and R_p than the simulated planet to maintain the character of the rest of the light curve.

Oblate planets that have impact parameters near the critical value, $b \sim 0.7$, cannot be fitted as easily using a spherical model because changes in the impact parameter of the fit cannot increase the duration of ingress and egress. For these planets, the difference between the oblate planet transit light curve and the best-fit spherical planet transit light curve is maximized, providing the largest possible photometric signal with which to measure oblateness.

At present, it is necessary to fit for R_* and stellar limb-darkening parameters because of our limited knowledge of these values for the host stars of transiting planets. If R_* was known to sufficient accuracy (less than 1%), then with knowledge of M_*, the degeneracy between R_*, R_p, and b would be broken, allowing measurement of planetary oblateness without fitting. However, without assumptions about the stellar mass, knowledge of R_* would only help to constrain M_*. Cody & Sasselov (2002) show that, for the star HD 209458, current evolutionary models combined with transit data serve to measure the stellar radius to a precision of only 10%.

In Figure 5, we plot the difference between the transit light curve of a hypothetical planet with the characteristics of HD 209458b but an oblateness $f = 0.1$ and that planet's best-fit spherical model fitting for R_*, R_p, b, and c_1. For low values of the impact parameter, $b \leq 0.5$, the best-fit spherical light curve emulates the oblate planet's ingress and egress while leaving a subtly different transit bottom due to the planet traversing a differently limb-darkened chord across the star. The magnitude of the difference is approximately a factor of 10 smaller than the nonfit difference from Figure 4. Near the critical impact parameter, $b = 0.7$, the transit light curve bottoms are very similar since the best-fit b is very similar to the actual oblate planet's impact parameter; however, the ingress and egress differ in flux by a few parts in 10^5 for $f = 0.1$. For grazing transits, $b \sim 1.0$, the best-fit spherical model's light curve is indistinguishable from the oblate planet transit light curve, even at the 10^{-6} relative accuracy level.

Figure 6 shows the same differences as in Figure 5 but with a second stellar limb-darkening parameter, BCGNB's c_2, also left as a free parameter in the fit. Including c_2 in the fit allows the fitting algorithm to match the transit bottom (the time between second and third contacts) better. This effect leads to excellent fits of oblate planet transits using spherical planet models and reduces the detectable difference to less than one part in 10^5 for $0.0 < b < 0.5$ and $b > 0.9$ using HD 209458 stellar and planetary radii and an oblateness of $f = 0.1$. For $b = 0.0$ and $b = 1.0$, the spherical model emulates an oblate transit particularly well, with the differences between the two being only a few millionths of the stellar flux.

In both the four- and five-parameter zero-obliquity models, it is easiest to measure the effects of oblateness on the transit light curve for transits near the critical impact parameter. For HD 209458 values with $f = 0.1$, the oblateness signal then approaches 3×10^{-5} for tens of minutes during ingress and egress and peaks near $b = 0.8$ instead of the critical value of $b = 0.7$ due to the finite radius of HD 209458b relative to its parent star.

Based on observations of the Sun, Borucki et al. (1997) expect the intrinsic stellar photometric variability on transit timescales to be $\sim 10^{-5}$. Jenkins (2002) used 5 yr of 3 minute resolution *Solar and Heliospheric Observatory* (*SOHO*) spacecraft data to deduce the noise power spectrum of the Sun. These noise effects are close enough in magnitude to the transit signal so as to affect the detectability of a transiting oblate planet.

Future high-precision, space-based photometry missions such as *Microvariability and Oscillations of Stars* (*MOST*) and Kepler may be able to detect the effect for highly oblate transiting extrasolar planets, but the signal-to-noise ratio could be so low as to make unambiguous measurements of oblateness difficult to obtain.

If an observer were to fit photometric time series data from a transit of an oblate planet without fitting explicitly for the oblateness f (as, for instance, if the precision is insufficient to measure f), the planet's oblateness will be manifest as an astrophysical source of systematic error in the determination of the other transit parameters. Figure 7 shows the effect that oblateness has on the stellar radius, planetary radius, impact parameter, and limb-darkening coefficient for HD 209458b. This variation is a strong function of the planet's impact parameter. In Figure 8, we show how this
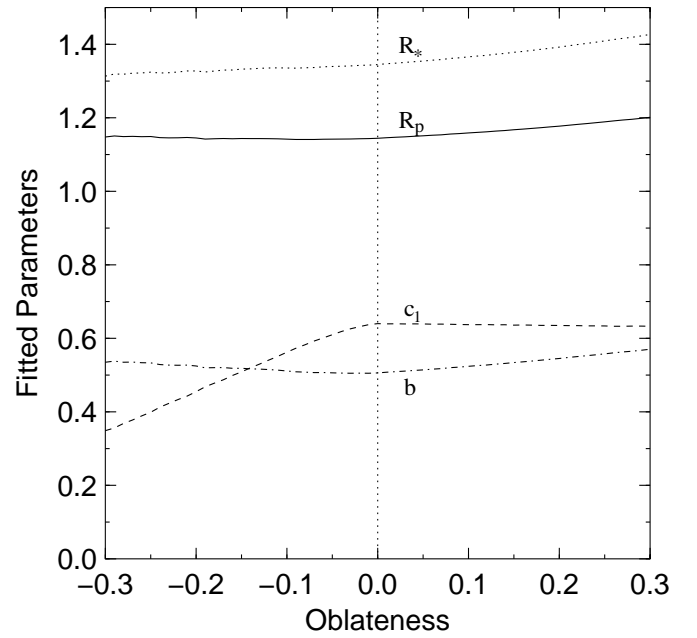

FIG. 7.—Best-fit parameters resulting from fitting a simulated transit light curve for a planet with oblateness f using a spherical planet transit model. Due to the degeneracy in measuring transit parameters R_*, R_p, and b, and oblateness f, the best spherical fit to the oblate data have larger radii and higher impact parameters than the actual values (see § 5.1). Objects with negative values of f are prolate, a physically unreasonable proposition that we include here for completeness.

systematic variation changes as a function of the initial impact parameter for the HD 209458b system. As a severe but still physical example, an HD 209458b–like planet with oblateness $f = 0.1$ that transits at $b = 0.0$ would be mea-
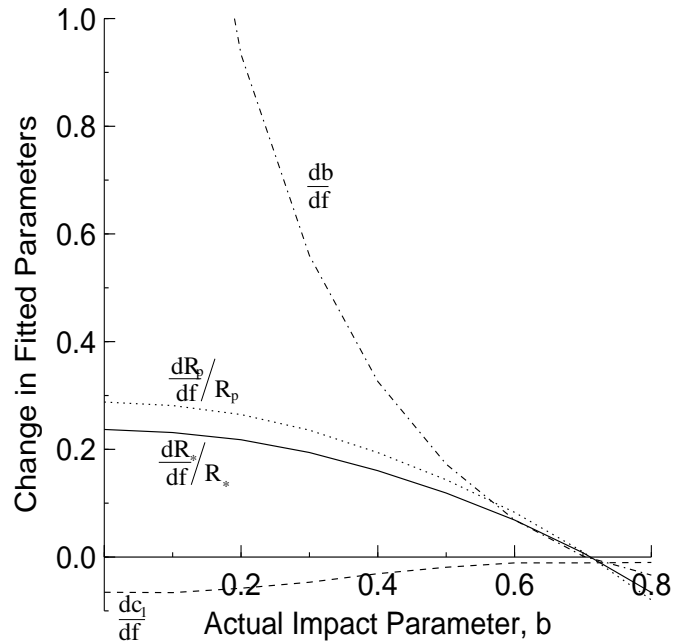

FIG. 8.—Here we plot the change of fitted spherical model parameters with oblateness as a function of impact parameter. The derivative of impact parameter with respect to oblateness continues off the top of this graph to 3.0 at $b = 0.0$. An oblate planet with zero obliquity transiting near the center of the star induces much higher deviations of the fitted parameters from the actual parameters than would a planet transiting near the critical impact parameter, $b = 0.707$.

sured to have radii 2% above actual and an impact parameter nearly 0.3 above the real impact parameter.

5.1.1. *HD 209458b*

To illustrate the robustness of the degeneracy between R_*, R_p, b, and f discussed in § 5.1, we fit the *HST* light curve from BCGNB using a planet with a fixed, large oblateness of 0.3(!). The best-fit parameters were $R_* = 1.08\ R_\odot$, $R_p = 1.26 R_{\mathrm{Jup}}$, $b = 0.39$, and $c_1 = 0.633$ with a reduced $\chi^2 = 1.06$—indistinguishable in significance from the spherical planet model! Although unlikely, a high actual oblateness for HD 209458b could alter the measured value for the planet's radius into better agreement with theoretical models.

The expected detectability of oblateness for HD 209458b is extremely low. During ingress and egress, the transit light curve for HD 209458b should differ from that of the best-fit spherical model by only one part in 10^6 for $f = 0.01$ and at the level of 3×10^{-7} if $f = 0.003$. For comparison, the BCGNB *HST* photometric precision is 1×10^{-4}.

Although the systematic error in the determination of transit parameters can be important for highly oblate planets, it is not at all significant for HD 209458b. Assuming HD 209458b has an oblateness of $f = 0.003$ as calculated in

§ 3, the fitted radii are only $\sim 0.05\%$ above the actual radii, and the fitted impact parameter is 0.0006 above what the actual impact parameter should be.

5.1.2. *OGLE-TR-56b*

Measuring the oblateness of the new transiting planet OGLE-TR-56b (Konacki et al. 2003), $f = 0.016$ (see § 3) would require photometric precision down to at least 4×10^{-6}. Since the impact parameter for this object is as yet unconstrained, the above precision corresponds to $b = 0.7$. For other transit geometries, higher precision photometry would be necessary to measure the oblateness of this object.

5.2. *Nonzero Obliquity*

We plot the detectability of oblateness and obliquity for planets with nonzero obliquity in Figure 9. Here we define the projected obliquity (hereafter referred to as just obliquity) or axial tilt t as the angle between the orbit angular momentum vector and the rotational angular momentum vector projected into the sky plane, measured clockwise from the angular momentum vector (see Fig. 3). The major effect of nonzero obliquity is to introduce an asymmetry into the transit light curve (Hui & Seager 2002).
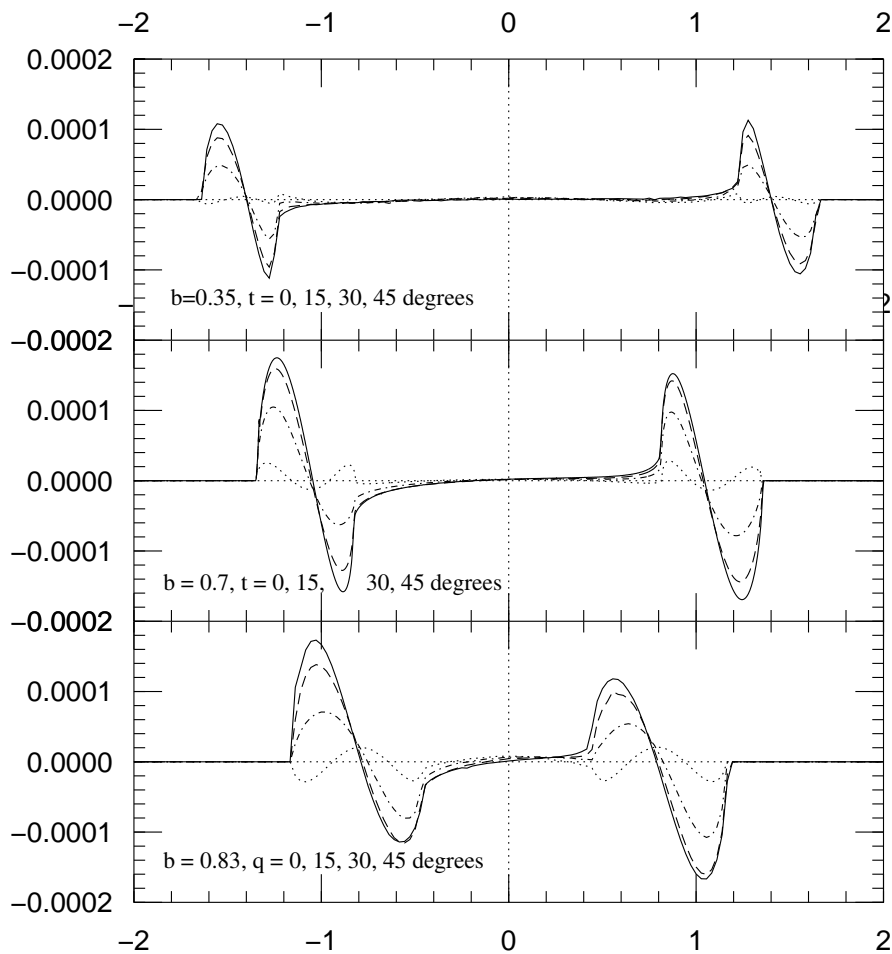

FIG. 9.—Detectability of oblateness and obliquity relative to the best-fit spherical model for planets with nonzero obliquity. *Top panel*: Detectability difference for $b = 0.35$ and $t = 0°$ (*dotted line*), $t = 15°$ (*dot-dashed line*), $t = 30°$ (*dashed line*), and $t = 45°$ (*solid line*). *Middle panel*: Same varying obliquities calculated for $b = 0.7$. *Bottom panel*: Differences for $b = 0.83$. The shape of the difference is qualitatively similar for each case. The difference is maximized for $t = 45°$ and $b = 0.7$ and falls off as the parameters near $t = 0°$, $t = 90°$, $b = 0.0$, and $b = 1.0$. Due to the symmetry of the problem, obliquities the ones shown plus 90° are the time inverse of the differences shown.

The plots in Figure 9 are difference plots for planets with different obliquities and impact parameters, yet all have the same shape qualitatively. In trying to fit the asymmetric ingress and egress light curves, the best-fit spherical planet splits the difference between them. For planets with $0 < t < \pi/2$, this process yields a difference curve that initially increases as the spherical planet covers the star at a faster rate than does the oblate planet. Because of the asymmetric nature of the problem, however, the egress of the oblate planet takes longer than the spherical one, causing an initial upturn near third contact. The transit light-curve difference for planets with $0 > t > -\pi/2$ is equal to the one for $0 < t < \pi/2$ but reversed in time.

This general shape is the same for the asymmetric component of each transit light curve, and it is superposed on top of the symmetric component studied in § 5.1. The asymmetric component is maximized near the critical impact parameter ($b = 0.7$) because the planet crosses the stellar limb with its projected velocity vector at an angle of $\pi/4$ with respect to the limb. For transits across the middle of the star, $b = 0$, the asymmetric component of the light curve vanishes as a new symmetry around the planet's path is introduced, and the local angle between the velocity vector and the limb is $\pi/2$. Similarly the asymmetric planet signal formally goes to zero for grazing transits at $b = 1.0$ but, in practice, the asymmetric component is still high for Jupiter-sized planets.

Planets with obliquities of zero ($t = 0$) are symmetric and have no asymmetric light-curve component (see § 5.1). Likewise, planets with $t = \pi/2$ are also symmetric. The asymmetric component is maximized for planets with $t = \pi/4$.

Transiting planets with nonzero obliquity can break the degeneracy between transit parameters discussed in § 5.1. However, when the obliquity is nonzero a degeneracy between projected obliquity and oblateness is introduced: a measured asymmetric light-curve component of a given magnitude could be due to a planet with low oblateness but near the maximum detectability obliquity of $t = \pi/4$, or it could be the result of a more highly oblate planet with a lower obliquity. In this case, only a lower limit to the oblateness can be determined based on the oblateness for an assumed obliquity of $\pi/4$. This degeneracy can be broken with measurements precise enough to determine the symmetric light-curve component. In addition, transit photometry is able to measure the projected oblateness and obliquity only of such objects due to the unknown component of obliquity along the line of sight (Hui & Seager 2002). Therefore, the true oblateness is never smaller than the measured, projected oblateness.

The asymmetric transit signal of an oblate planet with nonzero obliquity could also be muddled by the presence of other bodies orbiting the planet. Orbiting satellites or rings could both introduce asymmetries into the transit light curve that may not be easily distinguishable from the asymmetry resulting from the oblate planet. Satellites around tidally evolved planets are not stable (Barnes & O'Brien 2002), and rings around these objects may prove to be difficult to sustain as well. However, objects that are not tidally evolved, those farther away from their parent stars, may potentially retain such adornments, and their effects on a transit light curve could be difficult to differentiate from oblateness.

Orbital eccentricity can also cause a transit light curve to be asymmetric. Although the eccentricity of HD 209458b is zero to within measurement uncertainty based on radial velocity measurements, future planets discovered solely by their transits may not have constrained orbital parameters. For these objects with unknown eccentricity, if the eccentricity is very high, then under some conditions, the velocity change between ingress and egress may be high enough to emulate the oblateness asymmetry discussed in this section. However, we do not explicitly treat that situation in this paper.

6. CONCLUSIONS

Examining a transiting planet's precise light curve can allow the measurement of the planet's oblateness and, therefore, rotation rate, beginning the process of characterizing extrasolar planets. To a reasonably close approximation (a few percent), the rotation rate of an extrasolar giant planets is related to the planet's oblateness by the Darwin-Radau relation. Measurements of a planet's rotation rate could constrain the tidal dissipation factor Q for those planets as well as possibly shedding light on the tidal dissipation mechanism within giant planets based on the spin-to-orbit ratios of tidally evolved eccentric planets.

The detectable effect of oblateness on the light curve of a planet with zero obliquity is at best on the level of a few parts in 10^5. This effect may be discernible from space with ultra high-precision photometry but could prove to be indistinguishable from stellar noise or other confounding effects. Accurate independent measurements of stellar radius can break the degeneracy between the stellar radius, planetary radius, and impact parameter, allowing for much easier measurement of oblateness. Without such measurements, the primary effect of oblateness and zero obliquity when studying transit light curves will be to provide an astrophysical source of systematic error in the measurement of transit parameters.

Planets with nonzero obliquity have higher detectabilities (up to $\sim 10^{-4}$) than planets with no obliquity but yield nonunique determinations of obliquity and oblateness. In order to obtain unique obliquities and oblatenesses for these objects, precision comparable to that needed for the zero obliquity case is needed.

The detectability of oblateness for transiting planets is maximized for impact parameters near the critical impact parameter of $b = 0.7$. Many transit searches are currently underway, yielding the potential for the discovery of many transiting planets in coming years. Given the opportunity to attempt to measure oblateness, our analysis suggests that the optimal observational target selection strategy would be to observe planets around bright stars that transit near an impact parameter of 0.7.

REFERENCES

Barnes, J. W., & O'Brien, D. P. 2002, ApJ, 575, 1087
Borucki, W. J., Koch, D. G., Dunham, E. W., & Jenkins, J. M. 1997, in ASP Conf. Ser. 119, Planets beyond the Solar System and the Next Generation of Space Missions, ed. D. A. Soderblom (San Francisco: ASP), 153
Brown, T. M., Charbonneau, D., Gilliland, R. L., Noyes, R. W., & Burrows, A. 2001, ApJ, 552, 699
Charbonneau, D., Brown, T. M., Latham, D. W., & Mayor, M. 2000, ApJ, 529, L45
Claret, A. 2000, A&A, 363, 1081
Cody, A. M., & Sasselov, D. D. 2002, ApJ, 569, 451
Fortney, J., & Hubbard, W. 2002, Icarus
Goldreich, P., & Peale, S. J. 1968, ARA&A, 6, 287
Goldreich, P., & Soter, S. 1966, Icarus, 5, 375
Greenberg, R., & Weidenschilling, S. J. 1984, Icarus, 58, 186
Guillot, T., Burrows, A., Hubbard, W. B., Lunine, J. I., & Saumon, D. 1996, ApJ, 459, L35
Henry, G. W., Marcy, G. W., Butler, R. P., & Vogt, S. S. 2000, ApJ, 529, L41
Hubbard, W. B. 1984, Planetary Interiors (New York: Van Nostrand Reinhold)

Hubbard, W. B., Fortney, J. J., Lunine, J. I., Burrows, A., Sudarsky, D., & Pinto, P. 2001, ApJ, 560, 413
Hubbard, W. B., & Marley, M. S. 1989, Icarus, 78, 102
Hui, L., & Seager, S. 2002, ApJ, 572, 540
Jenkins, J. M. 2002, ApJ, 575, 493
Konacki, M., Torres, G., Jha, S., & Sasselov, D. 2003, Nature, 421, 507
Lissauer, J. J. 1993, ARA&A, 31, 129
———. 1995, Icarus, 114, 217
Lissauer, J. J., Berman, A. F., Greenzweig, Y., & Kary, D. M. 1997, Icarus, 127, 65
Marcy, G. W., Cochran, W. D., & Mayor, M. 2000, in Protostars and Planets IV (Tucson: Univ. Arizona Press), 1285
Murray, C. D., & Dermott, S. F. 2000, Solar System Dynamics (New York: Cambridge Univ. Press)
Peale, S. J. 1999, ARA&A, 37, 533
Press, W. H., Teukolsky, S. A., Vetterling, W. T., & Flannery, B. P. 1992, Numerical Recipes in C: The Art of Scientific Computing (New York: Cambridge Univ. Press)
Seager, S., & Hui, L. 2002, ApJ, 574, 1004
Showman, A. P., & Guillot, T. 2002, A&A, 385, 166
Ward, W. R., & Hamilton, D. P. 2002, BAAS, 34, 2908